Monte Carlo and Navier-Stokes Simulations of Compressible Taylor-Couette Flow

Bénédicte Larignon*, Kevin Marr† and David B. Goldstein‡
The University of Texas at Austin, Austin, TX, 78712

The compressible Taylor-Couette flow between concentric cylinders, in the case where the inner cylinder is rotating and the outer one is at rest, has been computed using a Direct Simulation Monte Carlo (DSMC) method and a pseudo-spectral/finite difference method. Depending on the air gap pressure, the flow in between the cylinders may be characterized by a variety of flow regimes ranging from free molecular to continuum, laminar to turbulent flow and by the presence of steady or unsteady toroidal vortices. In related new experiments performed by the Center for Electromechanics at the University of Texas at Austin, the pressure ranged from about 10 Pa to 1000 Pa. For the low-pressure cases (~10 Pa) the experiments are compared to the DSMC results while the high-pressure cases (~1000 Pa) are compared to the Direct Numerical Simulation results. For the intermediate cases (~100 Pa), both methods are used. At Taylor numbers of about 1-5, the velocity slips about 10% at the walls. At higher Taylor numbers between 10-50, the velocity slip decreases to about 1%, and at even higher Taylor numbers, the velocity profiles exhibit essentially no slip. Similarly, temperature slip at the walls decreases as the Taylor number increases. At low pressures, the velocity profile is roughly linear and the temperature profile has a parabolic shape. At high pressures, Taylor vortices are present in the gap and the axially averaged velocity profile evolves into an "S-shape" profile while the temperature parabola becomes flatter in the center of the gap. The simulated work required to rotate the inner cylinder and the heat flux to the walls are compared to experiments: agreement is good over the entire range of Taylor numbers.

Nomenclature

c_m	=	torque coefficient
d	=	gap width
H_{gap}	=	axial gap width
Kn	=	Knudsen number
P_2	=	pressure at the outer cylinder
r	=	position in the radial direction
Re	=	Reynolds number ($\equiv \rho_2 U_1 R_1 \mu_2^{-1}$)
R_1	=	radius of the inner cylinder
R_2	=	radius of the outer cylinder
$T(r)$	=	temperature at the radial position r
Ta	=	Taylor number ($\equiv \rho_2 U_1 d \mu_2^{-1} (d/R_1)^{1/2}$)
T_1	=	temperature of the inner cylinder
T_2	=	temperature of the outer cylinder
T_{axial}	=	"axial gap" torque
U_1	=	tangential velocity of the inner cylinder
$\bar{u}$	=	mean tangential velocity
$u(r)$	=	tangential velocity at the radial position r
z	=	position in the axial direction
κ	=	thermal conductivity
λ	=	molecular mean free path
μ	=	coefficient of viscosity
ν	=	kinematic viscosity
ρ_2	=	density at the outer cylinder
$\tau_{r\theta}$	=	shear stress in the radial dir. ($\equiv \mu(\partial \bar{u} / \partial r)$)
ω_1	=	angular velocity of the inner cylinder
ω_2	=	angular velocity of the outer cylinder

* Research Assistant, Dept. of Aerospace Engineering and Engineering Mechanics, larignonb@mail.utexas.edu, AIAA Student Member.
† Research Assistant, Dept. of Aerospace Engineering and Engineering Mechanics, kmarr@mail.utexas.edu.
‡ Associate Professor, Dept. of Aerospace Engineering and Engineering Mechanics, david@cfdlab.ae.utexas.edu, AIAA Senior Member.

I. Introduction

TAYLOR-Couette flow between two concentric cylinders is a well-known and oft-studied fluid dynamic problem prominent in the development of rotating machinery. Recent experiments of a high-speed flywheel system, where the inner cylinder, the rotor, rotates while the outer cylinder, the stator, is at rest, have been performed at the Center for Electromechanics at the University of Texas (UT-CEM).[1] Because of advances in composite materials, it is now feasible to build rotors that can sustain higher tip speed and, hence, higher Mach numbers. The experiments ran at high tip speed, up to Mach 2, and covered a wide pressure range. Due to viscous flow in the air gap between the rotor and stator, the pressure was kept low in order to reduce frictional losses. However, maintaining a vacuum low enough to negate such effects may be impractical in mobile flywheel applications where there are air leaks through the bearings. For that reason, the flow regimes ranging from free molecular to continuum, characterized by the presence or absence of steady toroidal vortices, have been studied in the present work.

Taylor investigated the formation of vortices in viscous flow between rotating concentric cylinders. He found that if the flow reaches a particular Reynolds number, toroidal ring vortices begin to develop.[2] The development of Taylor vortices can be predicated by means of a Taylor number, Ta, which is a non-dimensional measure of the gap width times the Reynolds number, Re. Depending upon the value of the Taylor number, a flow can exhibit several flow states including – simple laminar Couette flow, laminar Couette flow with either sinuous or straight steady Taylor vortices, laminar Couette flow with unsteady Taylor vortices, or turbulent flow superimposed on Taylor-like vortices.[3] Transitions between these different flow modes correspond to changes in the torque and heating on the inner and outer cylinders. Hence, predicting these transitions becomes important.

In the machines envisioned, the gas pressure in the air gap will be reduced well below atmospheric. Since the gas has a low-density, the molecular mean free path, λ, may be large relative to the gap width, d; therefore, the Knudsen number based on gap spacing, λ/d, may also be large. The resulting flow is described by the Boltzmann equation and characterized by velocity and temperature slip between the gas and the solid surfaces. The most common engineering approach for modeling such low-density flows is the Direct Simulation Monte Carlo (DSMC) method. In the DSMC method, flow properties such as temperature and velocity are determined by sampling a large number of simulated molecules. These molecules are systematically moved, allowed to collide with each other and with the boundaries before being moved again.[4] Several groups have used DSMC to explore Taylor-Couette flow in a rarefied or low-density gas. Rarefaction effects may significantly affect the development of Taylor-Couette vortices, but the flow regime has not been fully explored by either computational or experimental methods. At larger Knudsen numbers the flow characteristics become difficult to predict due to slip flow conditions at the rotor and stator walls. Riechelmann and Nanbu,[5] for example, established good agreement between torques calculated from DSMC simulations and experimental data for Knudsen numbers ranging between 0.004 and 0.04. They also found that vortex development changes the velocity in the middle of the gap by 35% and increases the slip at the walls by 5%. In a follow-up study three years later, they simulated wavy Taylor-Couette flow showing that the sinuous vortices move in an azimuthal direction and that the azimuthal wavelength corresponds to experimental observations.[6] In a study by Stefanov and Cercignani,[7] DSMC simulations clearly exhibit the onset of vortices at Taylor values higher than the incompressible critical value. In a separate investigation, Aoki et al[8] found that increasing the temperature difference between the surfaces of the cylinders increases the region of steady Couette flow.

Guaranteeing low pressures in the air gap is difficult, and the possibility of a pressure leak is real. Therefore, high-pressure continuum cases are also considered. Generally, experiments cannot provide a complete description of the interaction of these vortex structures with the surface, and numerical simulation of the governing Navier Stokes equations is necessary. The high-pressure regime is simulated using a Compressible Temporal DNS code (or CTDNS code) obtained from the University of Arizona. A companion paper,[9] also presented in this conference, describes the direct numerical simulations of flows in the continuum regime where the air gap pressure is above about 100 Pa. Numerous experimental and numerical studies have been developed to consider the influence of the geometry, the speed of the cylinders, the temperature of the walls, and the fluid compressibility on the onset of the instability. This onset is generally characterized by a critical Taylor number, Ta_c, defined as the largest value of the Taylor number such that all the axisymmetric disturbances in the flow are damped out. Swinney[10] compiled values of the critical Taylor number obtained by different sources. This set of data showed that Ta_c decreases as the radius ratio increases. Chandrasekhar[11] determined that the critical Taylor number decreases as the rotation rate ratio, ω_2/ω_1, decreases from 1 to 0. Hatay et al.[12] studied the influence of compressibility on the stability of the Couette flow between rotating cylinders. They found that for a resting outer cylinder, compressibility stabilizes the modes of the instability in the case of a narrow gap but destabilizes the modes for a wide gap. Finally, in both cases, they noticed that heating the outer cylinder has a stabilizing effect on the modes of the instability.

The purpose of the present study is to understand the characteristics of the flow in the UT-CEM flywheel air gap and to predict the resulting torques and heat fluxes on the rotor and stator surfaces. The numerical simulations encompass the rarefied flow regime where stable laminar Couette flow is expected and the continuum flow regime where Taylor vortex formation occurs. The bulk of the simulations are meant to emulate flywheel spin tests of a generic compulsator configuration conducted by the UT-CEM with air gap pressures of 10, 100, and 1000 Pa.[1] The work may also be considered a baseline study, preliminary to the examination of more complex flows involving, say, corner flows, abrupt changes in rotor speed or gas pressure, solid surface textures, or contamination by lubricant vapors.

A. Theory

A shear flow develops in a fluid-filled gap between two coaxial differentially rotating cylinders. For our purposes, both cylinders are long, and the inner cylinder rotates at a constant angular velocity while the outer cylinder is stationary. For incompressible flow, a common form of the Taylor number is[3]

$$\mathrm{Ta} = \frac{U_1 d}{\nu}\sqrt{\frac{d}{R_1}} \tag{1}$$

If the flow is incompressible and temperature variations are small (so the transport coefficients are approximately constant), simple laminar cylindrical Couette flow occurs when the Taylor number is less than 41.3. The Couette flow is characterized by a nearly linear velocity profile that spans the velocity range from zero at the stator to U_1 on the rotor surface.[3] The tangential velocity, u(r), in the gap can be found by solving the Navier-Stokes equations[13] as:

$$\frac{u(r)}{U_1} = \left(\frac{R_2}{r} - \frac{r}{R_2}\right)\left(\frac{R_2}{R_1} - \frac{R_1}{R_2}\right)^{-1} \tag{2}$$

The tangential velocity profile is normalized by the surface velocity of the rotor, and the curve of the velocity profile is determined by the ratio of the radius of the inner cylinder, R_1, and the outer cylinder, R_2. The radial position, r, is referenced from the axis of rotation.

To compute small temperature changes, the temperature distribution at a point in the gap, T(r), resulting from viscous dissipation is[13]

$$T(r) - T_1 = \left[\frac{\mu U_1^{\,2}}{\kappa\left(T_2 - T_1\right)}\frac{R_2^4}{R_2^4 - R_1^4}\left(1 - \frac{R_1^2}{r^2}\right)\left(1 - \frac{\ln\left(r/R_1\right)}{\ln\left(R_2/R_1\right)}\right) + \frac{\ln\left(r/R_1\right)}{\ln\left(R_2/R_1\right)}\right]\left(T_2 - T_1\right) \tag{3}$$

Above a Taylor number of 41.3, the laminar Couette flow becomes unstable. The resulting Taylor vortices are steady toroidal vortex cells having alternate rotation directions. As the Taylor number increases past 400, Taylor vortices develop unsteady 3-D motion, and eventually the flow becomes turbulent. For compressible flow, at elevated Mach numbers, the Taylor number ranges for each flow state may be different from those in the incompressible case.

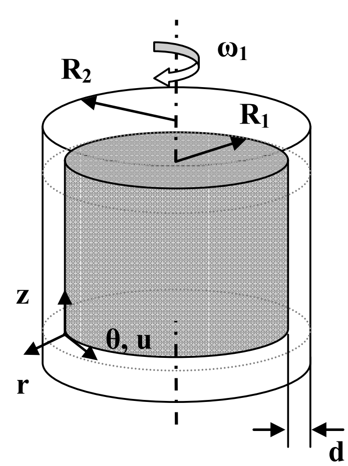

Figure 1. Flywheel schematic with stretched scale for clarity.

B. Domain and experimental data

The domain of interest is the whole gap between the two finite concentric cylinders (Fig. 1). However, the flow physics in the radial and the axial gaps is very different and the CTDNS and DSMC codes are presently only used to simulate the flow in the radial gap and effects at the ends of the cylinder are not simulated. However, in order to compare the numerical results to the experimental results, analytical formulas[14] have been used to model the flow in the axial gap. Even so, it was found that the torque exerted by the flow in the wide axial gaps is generally small compared to the torque produced in the radial gap.

The experiments done by UT-CEM aimed to measure the torque and the temperature distribution about a high-speed composite rotor in a stator structure. Hahne et al.[1] were using a composite flywheel that could sustain rotor speeds in excess of 40,000 rpm and rotor tip speeds of 900 m/s with pressure ranges from 10 Pa to 1000 Pa in the radial gap.

The different tests made with this flywheel varied in peak rpm, runtime and operating pressure. A total of 12 tests, numbered Tests #1 to 12, have been run with three different peak speeds of 15,000, 27,600 and 40,000 rpm and the three pressure levels of 10, 100, and 1000 Pa. Due to mechanical stress and thermal heating the inner radius and the gap width are different at each rpm. The input parameters for the numerical simulations of Test #3 to 12, presented in Table 1, have been extracted at one point in time near peak rpm from the experimental data.[1]

Table 1. Experimental data used for the simulations. The centrifugal and thermal stresses are accounted for in the rotor diameter. The radial gap pressure is measured in the middle of the radial gap at the stator while the rotor and stator temperatures are the average temperatures measured by multiple sensors in the radial gap.

CEM TEST #		3	4	5	6	7	8	9	10	11	12
Inner radius, R_1	m	0.2125	0.2122	0.2122	0.2125	0.2125	0.2122	0.2125	0.2122	0.213	0.213
Gap width, d	m	0.0031	0.0034	0.0034	0.0031	0.0031	0.0034	0.0031	0.0034	0.0025	0.0025
Radial gap pressure, P_2	Pa	155	121	1463	1796	20	14.7	1746	13.3	26.7	241
Axial gap pressure, P	Pa	113	106	1309	1317	9.3	8.0	1264	8.0	8.0	126
Rotor speed, ω_1 or U_1	rpm	27600	15000	15000	27600	27600	15000	27600	27600	40000	40000
	m/s	614	333	333	614	614	333	614	333	892	892
Rotor temperature, T_1	K	348	321	338	351	344	315	347	336	344	344
Stator temperature, T_2	K	350	318	339	366	344	315	362	333	368	358
Taylor Number, Ta	–	17	10	107	181	3.6	1.6	179	1.5	5.0	27

II. Computational Approach

A. Direct Simulation Monte Carlo (DSMC)[15,16]

The DSMC method moves model molecules and samples molecular collisions to simulate a gas flow. The overall DSMC method is a sequence of move-collide operations described by Bird[4].

The simulation area is an axisymmetric wedge in which the dominant mean flow is perpendicular to the simulation plane. The z-axis of rotation is parallel to the axis of the cylinder and along the rotor surface; the r-axis is positioned so that the positive direction is radially out. The sides of the domain are the inner and outer cylinder surfaces, and the top and bottom are planes of symmetry. Molecular collisions with the rotor and stator surfaces are governed by diffuse

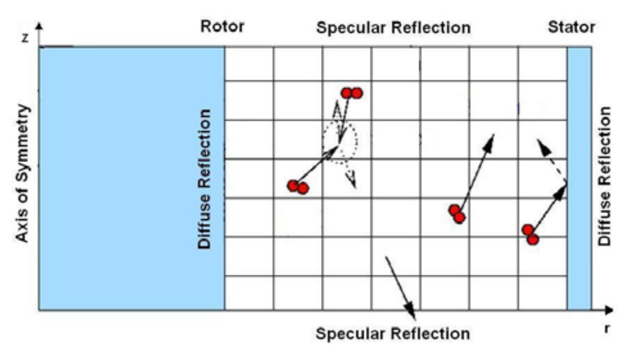

Figure 2. DSMC computational domain.

reflection at the respective surface temperatures – molecular velocity after the reflection is independent of the velocity before the reflection (Fig. 2). The plane of symmetry boundaries are defined by specular reflection resulting in a mirror image of the flow about the boundaries. For present purposes, molecular collisions are simulated with the variable hard sphere (VHS) model. The velocity dependent collision cross section is adjusted to produce the correct temperature exponent of the coefficient of viscosity of diatomic nitrogen gas.[4] To ease the DSMC calculations, the numerical gap is filled with simulated nitrogen even if the experimental gap is filled with air. A numerical comparison between the air and nitrogen-filled gap showed that the resultant torque differs by less than 5%.

The simulation area is divided into identical rectangular cells to form the grid pattern. The radial span of each cell is no more than one mean-free path, and the FNUM ratio, the ratio of real molecules to simulated molecules, is set so that there are approximately ten simulated molecules per cell.

To initialize the flow, mean number density corresponding to a measured pressure from each UT-CEM Test is specified for the gas (ideal nitrogen). The rotor is given a certain surface velocity, which is applied as if the rotor instantaneously jumps to the specified speed at time zero.

Convergence for time-step size, steady state and spatial grid resolution is verified for each run.

B. Compressible Temporal Direct Numerical Simulation code (CTDNS)

The code used for the direct numerical simulations is a Compressible, Temporal code (CTDNS) developed at the University of Arizona.[9,17] It solves the three-dimensional compressible Navier-Stokes equations in conservative form using a pseudo-spectral/finite difference approach in space and a Runge-Kutta scheme in time. Additional constitutive relations are employed to close the governing equations, namely, the equation of state for ideal gas for computing the pressure, the Newtonian fluid assumption for the viscous stress, Fourier heat conduction for the heat flux, and Sutherland's law for the dependence of viscosity and conductivity on the temperature. The governing equations are solved in cylindrical coordinates inside the annular computational domain shown in Fig. 1 using a pseudo-spectral decomposition in the axial (z) and the azimuthal (θ) directions. In the radial direction (r), sixth-order split compact differences are employed on a non-uniform grid with points clustered near the rotor and stator walls. An explicit, fourth-order Runge-Kutta scheme is used for time-advancement. While in the axial and azimuthal directions periodicity is assumed for all flow variables, in the radial direction, at the rotor / stator boundaries, no-slip conditions for the velocities and isothermal boundary conditions for the temperature can be imposed. A convergence study has been done and is presented in the companion paper.[9]

III. Results

The numerical results presented in this section are obtained once the flow reaches steady state. In the low-pressure cases up to 100 Pa, no vortices develop and the parameters in the gap are only dependent on the radial position. In the high-pressure cases, the parameters depend also on the axial position and they are plotted in the (r, z) plane. For a better comparison between low and high-pressure results, axially averaged values of the parameters versus the radial position are also examined for the high-pressure cases. The profiles of the flow parameters are only plotted for one Test case for each pressure range, each case typical of each class of flow: Test #7 for the low pressures (~10 Pa), Test #3 for the intermediate pressures (~100 Pa) and Test #6 for the high pressures (~1000 Pa).

A. Rarefied Couette flow

In this section, the results for the low-density regime at gap air pressures of about 10 Pa, in the Tests #7, 8, 10 and 11, are presented. The Taylor number range for these simulations is 1 to 5 and the Knudsen number is about 0.1. Radial position and velocity are non-dimensionalized, but temperature is left in dimensional form to more easily visualize the temperature slip near the walls.

The velocity profiles are roughly linear across the narrow gap, but show an increased gradient near the rotor and stator surfaces (Fig. 3). Non-dimensional velocity gradients are calculated by taking the slope of the velocity profiles at three locations along the gap: near the center of the gap, near the rotor surface, and near the stator surface (Table 2). The velocity gradients near the walls are approximately 50 to 60% larger than the gradient in the center of the gap. The DSMC simulations also show that the velocity near each surface slips or is different than the velocity of the surface itself. The amount of the velocity slip is quantified by comparing the velocity profiles to the no-slip analytical results. For all four low-pressure cases, the velocity slip ranges from 7-10% on both rotor and stator surfaces. However, Tests #8 and 10 show slightly more velocity slip on both surfaces than Tests #7 and 11.

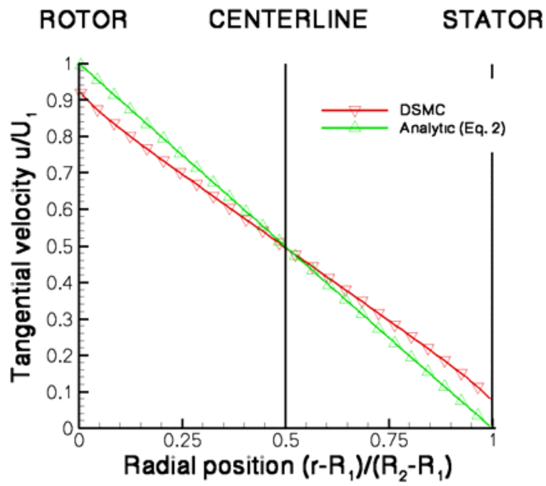

Figure 4. Velocity profile at 10 Pa (Test #7).

Table 2. Velocity gradient at 10 Pa.

CEM Test #	Absolute Value of the Velocity Gradient $= \left\lvert \dfrac{\partial\left(u/U_1\right)}{\partial\left(\frac{r-R_1}{R_2-R_1}\right)} \right\rvert$		
	Center	Rotor	Stator
7	0.8	1.2	1.2
8	0.77	1.2	1.2
10	0.76	1.1	1.1
11	0.81	1.3	1.3

The temperature profiles have a parabolic shape with the maximum temperature near the center of the gap (Fig. 4). In the cases where the temperature is the same at each wall, the profiles are nearly symmetric, while in the cases with a temperature difference between the rotor and the stator the profiles are slightly off-center. The relative steepness of the profiles also differs for each test case. For Tests #8 and 10, the parabola is quite flat, where the maximum temperature is about 2-3% hotter than the near-stator temperature. For Tests #7 and 11, however, the parabolic profile becomes steeper. Test #7 shows a temperature increase of 7% from near the stator to the center of the gap; Test #11 shows a slightly larger temperature increase of about 13%. The temperature increase is defined as the percent difference between the maximum temperature in the gap and the temperature just near the stator wall. Similar to the velocity profiles, the temperature profiles also exhibit slip characteristics where the flow just near the surface is hotter than the surface itself. Table 3 shows the slip percentage at each wall for each test case. The slip percentage is defined as the percent difference between the temperature near the wall and the wall surface temperature. Tests #8 and 10 show similar slip results; the temperature slip near the surface is close to 2% for both Test cases. Compared to Tests #8 and 10, the temperature slips about twice as much in Test #7 and about ten times more in Test #11. Test #11 was the only simulation that exhibited significant slip asymmetry, where the temperature slip near the rotor was larger than the slip near the stator. However, it is important to note that for Test #11, the stator is about 20 K hotter than the rotor. The other low-pressure simulations have only a small temperature difference between the rotor and stator.

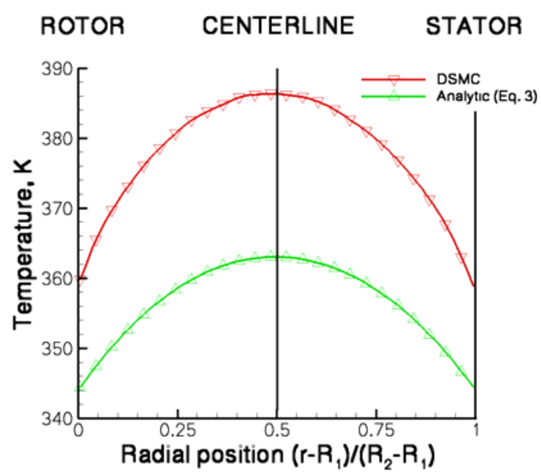

Figure 3. Temperature profiles at 10 Pa (Test #7).

Table 3. Temperature Slip at 10 Pa.

CEM Test #	Temperature Slip (%)	
	Rotor	Stator
7	4.7	4.7
8	1.6	1.6
10	1.8	1.8
11	10.2	7.3

B. Intermediate pressure (100 Pa)

The intermediate pressure simulations, in the Tests #3, 4 and 12, are run with gap pressures around 100 Pa with Knudsen numbers about 0.01 indicating nearly continuum flow. For that reason both CTDNS and DSMC simulations of these test have been made. The corresponding Taylor number range for these tests is between 10 and 30 (Table 1). From the theory[3], a laminar Couette flow regime is expected for Taylor numbers less than 41.3 in incompressible flow. The CTDNS and DSMC numerical simulations exhibit, indeed, a laminar flow with no Taylor vortices present.

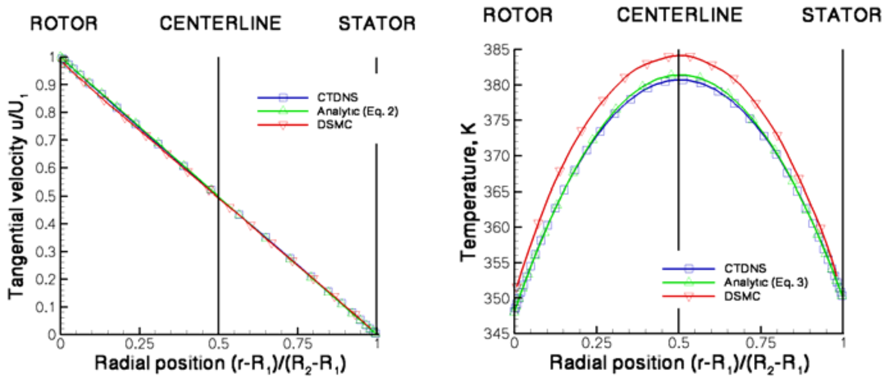

a) Tangential velocity b) Temperature

Figure 5. Comparison of the numerical and analytical profiles (Test #3).

The comparison between the numerical results, both DSMC and CTDNS, with the analytical solutions provided by Eqs. (2) and (3) is presented in Figs. 5a,b for both tangential velocity and temperature. Similar to the low-pressure simulations, the profile for the tangential velocity is nearly linear and the temperature profile is nearly parabolic with a maximum slightly closer to the hotter wall as seen in Figs. 5a,b. The agreement between the numerical results and the analytical solutions of Eqs. (2) and (3) is good. The CTDNS and analytical profiles are nearly the same for both temperature and velocity. However, the DSMC profiles exhibit temperature slip and a tiny velocity slip, which are not taken into account in both CTDNS and analytical results. For that reason, the DSMC velocity profile exhibit slightly steeper gradients at the walls and the DSMC temperature profile also present steeper gradients at the wall and a higher temperature in the middle of the gap.

Unlike the low-pressure tests, these velocity profiles do not show a significant velocity gradient increase near the two wall surfaces, and the velocity slip (about 1-2%) at each wall is much smaller. The velocity gradient is about 0.97 for all three medium pressure simulations. However, the temperature profile behavior at medium pressure is almost identical to that at low pressure. The profiles exhibit slip characteristics and increased temperature in the center of the gap (Table 4). Similar to the low-pressure temperature slip results, the temperature slip is nearly the same for both wall surfaces. Also, as the rotor tip speed increases, the temperature slip and temperature increase in the gap increase as well.

Table 4. Gap temperature behavior at 100 Pa.

CEM Test #	Temperature Slip (%)		Temperature Increase (%)
	Rotor	Stator	
3	0.9	0.9	8.8
4	0.3	0.3	3.4
12	2.0	2.0	17.5

C. Taylor-Couette flow with vortices

Schlichting[3] suggests that as the Taylor number in incompressible flow ranges between 41.3 and 400, laminar flow with Taylor vortices would be observed. For increased pressures around 1000 Pa, in the Tests #5, 6 and 9, the Taylor numbers are in this range of values and Taylor vortices are found to be present in the CTDNS compressible flow simulations too. Figures 6a,b show contours of the tangential velocity in the (r, z) plane and its axially averaged profile for Test #6. In Fig. 6a, two vortices can be observed from the vector representation of velocity in (r, z) plane. The lower vortex turns clockwise and the upper one counterclockwise. On the right (Fig. 6b), the laminar linear profile has evolved into an “S-shape” curve in the axially averaged flow due to the presence of vortices in the gap.

The "S-shape" of the velocity profile characterizes a flow with a higher gradient at the walls due to the mixing induced by the vortices and a nearly flat region where the axially averaged velocities are nearly constant in the middle of the gap.

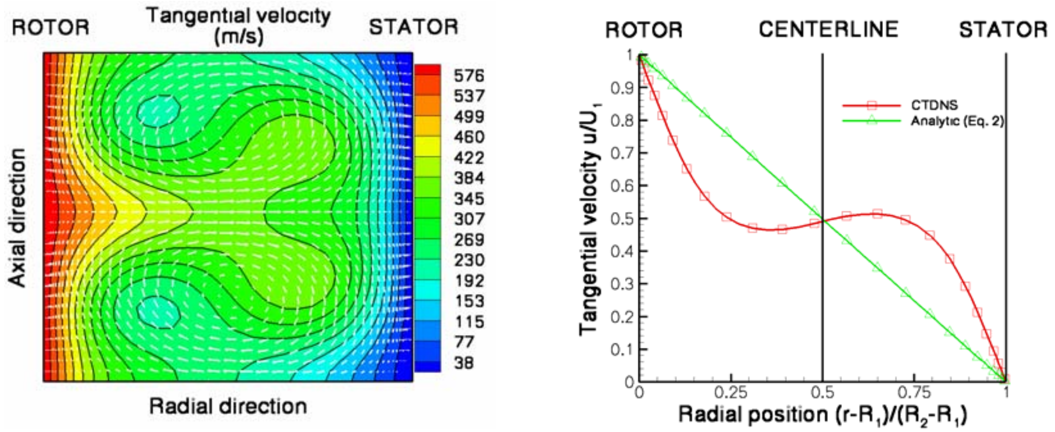

a) Tangential velocity contours

b) Axially averaged tangential velocity profile compared to simple analytic results

Figure 6. Tangential velocity contours in the (r, z) plane and accompanying (v, w) velocity vectors (left) and axially averaged tangential velocity profile (right) (Test #6).

In the higher-pressure cases the axially averaged temperature profile exhibits two peaks, the highest of which is closer to the hottest wall (Fig. 7b). The shape in the center of the gap is much flatter than in the laminar flows. This averaged shape also exhibits steeper gradients at the walls, which will induce a higher heat flux. All these changes are due to the presence of vortices that cause macroscopic radial mixing of the flow. In the case presented in Fig. 7a, the rotor is cooler than the stator. Between the vortex cores, the vortices move the low temperature fluid along the rotor wall toward the separation point in the middle of the gap. Simultaneously, at the top and bottom of the gap, the high temperature particles closer to the stator are moved away from the stagnation point. Alternate layers of hotter and cooler fluid can than be observed in the (r, z) plane and a mushroom form can be seen in the temperature contour. However, the shape obtained here is more complex than expected. For that reason, this run has been repeated a few times with various input temperatures and pressures. But the results appear to confirm that the flow represented in Fig. 7a is steady while the cause of this shape remains uncertain.

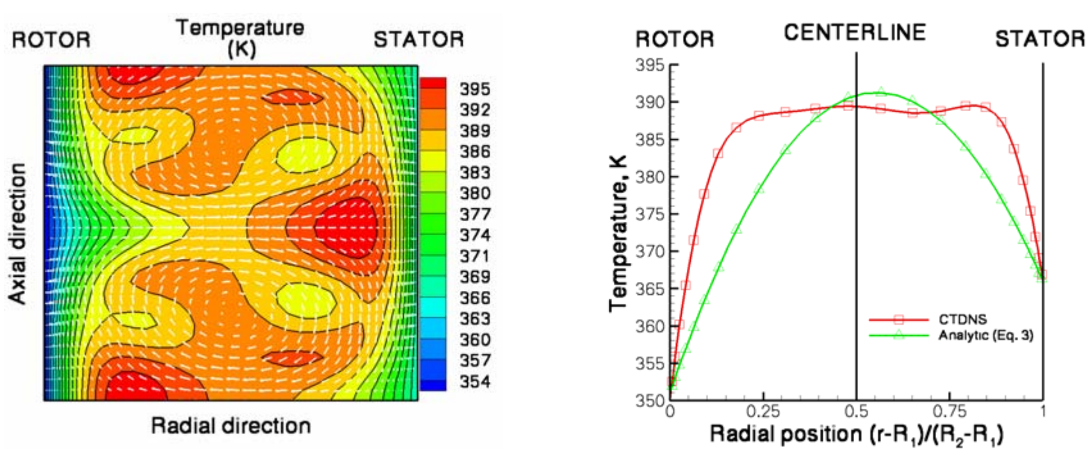

a) Temperature contours

b) Axially averaged temperature profile compared to simple analytic results

Figure 7. Temperature contours in the (r, z) plane and accompanying (v, w) velocity vectors (left) and axially averaged temperature profile (right) (Test #6).

The shear stress in the radial direction, $\tau_{r\theta}$, due to the mean tangential velocity exhibits a sinusoidal shape for the high-pressure cases (Fig. 8b). Due to the increased gradient of the tangential velocity at the walls, the magnitude of the shear stress values at the wall is much higher in the high-pressure case. Yet, due to the general flatness of the velocity profile in the middle of the gap, the magnitude of the shear stress there is correspondly small. Moreover, the values of the shear stress at the rotor and at the stator are slightly different. The amplitude of this difference is such that the torque is the same at both walls.

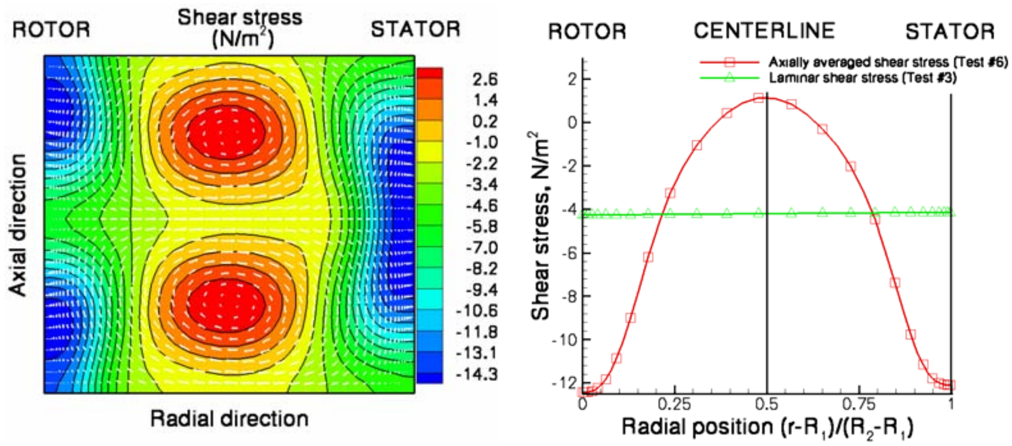

a) Shear stress $\tau_{r\theta}$ contours

b) Axially averaged shear stress $\tau_{r\theta}$ profile (Test #6) compared to laminar profile (Test #3)

Figure 8. Shear stress $\tau_{r\theta}$ contours in the (r, z) plane and accompanying (v, w) velocity vectors (left) and axially averaged shear stress $\tau_{r\theta}$ profile (right) (Test #6).

In Fig. 9a, the heat flux contour shows three distinct regions. The region in the center of the domain exhibits a heat flux close to zero. In the region close to the rotor, which is the coolest wall in this case, the heat flux is negative everywhere (into the rotor) but is not uniform along the wall. In fact, the region near the separation point on the rotor presents a nearly zero heat flux. As shown in the temperature contours (Fig. 7a), the vortices move the cooler fluid from the rotor and mix it with the hotter fluid present in the center of the gap. In the stagnation region where the mid-gap fluid is moved to the wall, the heat flux is larger. The heat flux profile shows an "S-shape" for the higher-pressure cases. In the 1000 Pa cases, the "flatter" region in the center of the gap observed in the temperature profile (Fig. 7b) induces the "S-shape" of the heat flux profile while the higher temperature gradients at the walls lead to higher values of heat flux at the walls compared to the lower pressure cases.

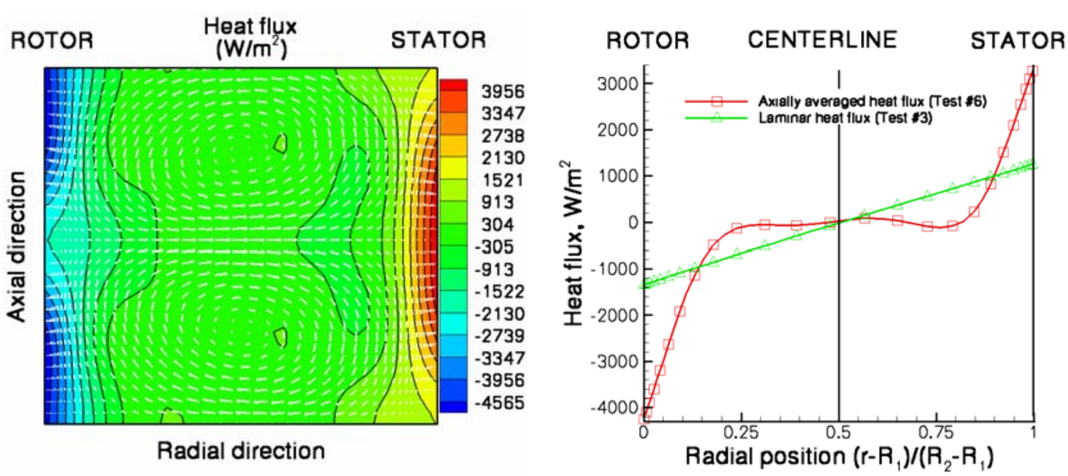

a) Heat flux contours

b) Axially averaged heat flux profile (Test #6) compared to laminar profile (Test #3)

Figure 9. Radial heat flux contours in the (r, z) plane and accompanying (v, w) velocity vectors (left) and axially averaged radial heat flux profile (right) (Test #6).

D. Torque, power and heat flux: comparison to the experiments

For each DSMC and CTDNS simulation, the torque and the heat flux at the walls are calculated and the torque is compared to the UT-CEM experimental results (Tables 5 and 6). The numerical torque only considers the radial air gap flow. However, the torque measured during the experiments also takes into account the torque due to the axial gap flow on the top and the bottom of the rotor. In order to compare the numerical results to the experimental ones, this "axial gap" torque must be added to the numerical torque. An empirical solution given in "*The General Electric Fluid Flow Data Book*" (1994) is used. This book reviews some empirical methods that can be used to estimate the torque on rotating disks and rotating cylinders using a curve fit to experiments. In our case, we are interested in modeling completely enclosed rotating disks to calculate the torque due to the axial air gap flow. For the "axial gap" torque, the Reynolds number, and the ratio between the axial gap width (H_{gap}) and the rotor radius (R_1) give us the flow regime. We can then estimate the total torque coefficient and finally the torque. In the experiments, the ratio H_{gap}/R_1 is constant and is about 0.06. In this case, the torque is given by Eq. (4).

$$T_{axial} = c_m \, \rho_2 \, U_1^2 R_1^3 \tag{4}$$

where the torque coefficient is fit as

$$\text{if Re>1500} \quad c_m = \frac{1.85\left(\dfrac{H_{gap}}{R_1}\right)^{1/10}}{\sqrt{Re}} \tag{5}$$

$$\text{if Re<1500} \quad c_m = \frac{\pi}{\left(\dfrac{H_{gap}}{R_1}\right) Re} \tag{6}$$

It must be noticed that Eqs. (4) to (6) involve the density at the stator. The density will be deduced from the pressure by using the perfect gas law. For the empirical calculations in the axial air gap the pressure that is used is the pressure measured near the axis of the rotor.

Table 5. Torque calculations (in Nm). The radial gap only values are obtained directly from the numerical simulations where the flow is only simulated between the cylinder walls. The radial and axial gap values are obtained by adding the torque at the bottom and at the top of the rotor, calculated using the *"The General Electric Fluid Flow Data Book"*, to the previous numerical values.

CEM Test #	Radial Gap Only		Radial and Axial Gap		Measurement
	DSMC	CTDNS	DSMC	CTDNS	
3	0.161	0.146	0.226	0.211	0.198
4	0.072	0.065	0.097	0.090	0.086
5	—	0.166	—	0.254	0.244
6	—	0.423	—	0.643	0.705
7	0.119	—	0.140	—	0.147
8	0.051	—	0.062	—	0.068
9	—	0.420	—	0.637	0.703
10	0.056	—	0.067	—	0.070
11	0.233	—	0.261	—	0.254
12	0.316	0.268	0.436	0.388	0.424

The analytically adjusted DSMC torque results compare favorably with the experimental UT-CEM results. At 10 Pa, the DSMC simulations are at worst 8% (Test #8), at best 3% (Test #11) and on average 5% (Tests #7 and 10) less than the experimental torque measurements. In general, the 100 Pa DSMC results did not agree quite as well as the 10 Pa results. At 100 Pa, DSMC Tests #3 and 4 simulations overestimate the experimental torque by 10%. Test #12, however, shows excellent (within 1%) agreement with experiments.

The agreement between CTDNS and experimental results is better for the low rotor tip speed regime (U_1 = 333 m/s), for both low (Test #4) and high (Test #5) pressures. The results obtained in Test #3 simulations also agree well with experiments where the velocity (U_1 = 614 m/s) and the pressure (P_2 = 100 Pa) are still low. In Tests #6 and 9, the differences are greater and the simulations underpredict the experimental torque.

It is important to notice that in reality, however, the pressure in the axial gap should vary with the distance from the axis of the cylinders and fall between the measured axis and radial gap pressures. In the numerical calculations, the axial gap pressure is taken to be equal to the pressure measured close to the axis of the cylinders, which is smaller than the radial gap pressure due to a centrifugal pressure gradient. This might be one of the reasons why the numerical torque underpredicts the experimental results.

Table 6. Numerical heat flux at the rotor and the stator for each Test case showing the percentage of heat dissipated through each wall. The values of the heat flux in the Table 6 for the Tests #3, 4, 5, 6, 9, and 12 are from the CTDNS runs whereas the values for the Test #7, 8, 10 and 11 are from the DSMC runs.

CEM TEST #		3	4	5	6	7	8	9	10	11	12
Heat flux (W/m^2)	To rotor: q_1	1345	297	829	4171	2311	494	4114	509	3029	3721
	To stator: q_2	1259	329	766	3314	1930	474	3314	521	2680	3256

Table 6 shows that the heat flux is greater to the cooler wall which is usually the rotor. Moreover, contrary to the torque results, the net heat flow may be different to the rotor and the stator. The conservation of energy in the simulations can be verified by comparing the power added to the flow trough the torque on the rotor, $P_{\text{radial flow}}$, with the heat flow to the walls, $Q_1 + Q_2$. Here, the subscript “radial flow” indicates simply the portion due to radial gap flow. The power $P_{\text{radial flow}}$ is calculated using the torque results while the heat flow to the wall is calculated using the heat flux simulations. By conservation of energy during steady state operation, we should have $P_{\text{radial flow}} = Q_1 + Q_2$. The CTDNS results give only very small non-zero errors which are likely due to round-off errors during the dimensionalization or slight residual flow unsteadiness and not to any flaw in the numerical dissipation.

IV. Conclusion and Outlook

The low-pressure numerical DSMC simulations where the flow is laminar are characterized by “S-shaped” velocity profiles, parabolic temperature profiles and slip conditions at the rotor and stator surfaces. At low Taylor numbers (1-5), the velocity profiles exhibit increased gradients near the wall surfaces and velocity slip at the 10% level. However, as the Taylor number increases (10-30), DSMC simulations show that the velocity gradient across the gap becomes constant, and the velocity slip is an order of magnitude less than at the low Taylor numbers. For both low and intermediate pressure regions, the temperature behavior within the gap is qualitatively similar. Both pressure regions show that as the rotor velocity increases about 300 m/s, the temperature slip and gap temperature difference approximately doubles. However, the temperature slip at low pressure is about five times larger than at high pressure for corresponding rotor tip speeds. The DSMC/Axial torque calculations agree reasonably well with experiments. At low pressures and Taylor numbers (1-5), DSMC underestimates the torque on average by 5%. At higher pressures (Taylor numbers between 10-30), DSMC overestimates the torque by about 10%. It is important to note that our method does not account for the torque aberrations due to the corner flow. It is possible that the 5-10% discrepancy could be resolved by including the corner flow. Also, the axial gap calculation assumes a spatially uniform pressure (no gradients in the axial gap), which is not true for the actual machine.

The CTDNS simulations also agree well with the experimental results and give good insight into the nature of the flow. For the intermediate pressure cases (Test #3, 4 and 12), the flow observed is laminar, and the results observed agree with the experimental and analytical results. The tangential velocity as well as the shear stress and the heat flux profiles exhibit a nearly linear shape while the temperature profile can be characterized by a parabola with a maximum slightly closer to the hotter wall.

In the high-pressure cases (Test #5, 6, 9), Taylor vortices are observed, and the axially averaged resulting profiles for each parameter evolves into more complex shapes. The tangential velocity, the shear stress and the heat flux have “S-shaped” profiles with a flatter zone in the middle of the gap. The temperature parabola becomes flatter in the center of the gap. The contours of the different parameters in the (r, z) plane also give information about the different zones that can be considered in the flow. The core of the vortices is a zone where the shear stress may be positive. The stagnation points on the wall present a high temperature which results in larger heat flux, and greater magnitude of shear stress. On the other hand, the separation points exhibit reduced heat flux and shear stress. In all cases, the difference between the numerical and experimental torque does not exceed 13%.

Acknowledgments

The authors gratefully acknowledge The University of Texas Center for Electromechanics for the partial funding of this research. We would like to also thank Dr. J. Zhang for the use of his DSMC code[15,16] and his helpful discussions.

References

[1]Hahne, J. J., Werst, M., Penney, C., Liu, H.P., O'Harden, J., and Bogard, D., "Measurement of Windage Losses and Temperature Distribution for a High Speed Composite Rotor in a Stator Assembly at Low Air Pressures," *ASME 2003*-47117, July 2003.

[2]Taylor, G.I., *Mechanics of Fluids Miscellaneous Papers IV*, Cambridge University Press, London, 1971, pp34-85.

[3]Schlichting, H., *Boundary-Layer Theory*, 7th ed., McGraw-Hill, Inc., New York, 1979, Chaps. 5 and 17.

[4]Bird, G.A., *Molecular Gas Dynamics and the Direct Simulation of Gas Flows*, Clarendon Press, Oxford, 1994.

[5]Riechelmann, Dirk and Nanbu, Kenichi. "Monte Carlo Direct Simulation of the Taylor Instability in Rarefied Gas," *Phys. Fluids A*, Vol. 5, No. 11, Nov 1993, pp. 2585-2587.

[6]Riechelmann, D., and Nanbu, K., "Three-dimensional Simulation of wavy Taylor Vortex Flow by Direct Simulation Monte Carlo Method," *Phys. Fluids*, Vol. 9, No. 4, Apr 1997, pp. 811-813.

[7]Stefanov, S., and Cercignani, C., "Monte-Carlo Simulation of the Taylor-Couette Flow of a Rarefied Gas," *Journal of Fluid Mechanics*, Vol. 256, pp. 199-213.

[8]Aoki, K., Sone, Y. and Yoshimoto, M. "Numerical Analysis of the Taylor-Couette Problem for a Rarefied Gas by the Direct Simulation Monte Carlo Method," *Proc. of the 21st International Symposium on Rarefied Gas Dynamics*, Vol. 2, July 1998, pp. 109-116.

[9]Larignon, B., Wernz, S., Goldstein, D., and Fasel, H., "Numerical Investigation of Vortex Onset in Supersonic Taylor-Couette Flow," *43rd AIAA Aerospace Sciences Meeting and Exhibit*, January 2005, AIAA Paper AIAA-2005-517.

[10]Swinney, H.L., "Hydrodynamic Instabilities and the Transition to Turbulence," edited by H. L. Swinney and J. P. Gollub. Springer, Berlin, 1981, pp. 139-180.

[11]Chandrasekhar, S., *Hydrodynamic and Hydromagnetic Stability*, Clarendon Press, Oxford, 1961.

[12]Hatay, F.F., Biringen, S., Erlebacher, G., Zorumski, W.E., "Stability of High-Speed Compressible Rotating Couette Flow," *Phys. Fluids*, Vol. 5, No. 2, February 1993, pp. 393-404.

[13]White, F., *Viscous Fluid Flow*, 2nd ed., McGraw-Hill, Inc., New York, 1991, pp. 110-112.

[14]"The General Electric Fluid Flow Data Book," Genium Publishing Corporation, New-York, 1994.

[15]Zhang, J., Goldstein, D., Varghese, P., Gimelshein, N., Gimelshein, S., Levin, D., Trafton, L., "DSMC Modeling of Gas Dynamics, Radiation and Fine Particulates in Ionian Volcanic Jets," *Proc. of the 23rd International Symposium on Rarefied Gas Dynamics*, Vol. 663, 2003, pp. 704-711.

[16]Zhang, J., Goldstein, D., Gimelshein, N., Gimelshein, S., Levin, D., Varghese, P., "Modeling Low Density Sulfur Dioxide Jets: Application to Volcanoes on Jupiter's Moon Io," *35th AIAA Thermophisics Conference,* June 2001, AIAA-2001-2767.

[17]Larignon, B., "Numerical Simulations of the Compressible Flow between Concentric cylinders using an External Force Field in a Pseudo-spectral Code," Master Thesis, Aerospace Engineering Dept., University of Texas, Austin, Tx, 2004.